

Multicomponent MR fingerprinting reconstruction using joint-sparsity and low-rank constraints

Martijn Nagtegaal¹ | Emiel Hartsema¹ | Kirsten Koolstra² | Frans Vos^{1,3}

¹Department of Imaging Physics, Delft University of Technology, Delft, The Netherlands

²Division of Image Processing, Department of Radiology, Leiden University Medical Center, Leiden, The Netherlands

³Department of Radiology, Erasmus MC, Rotterdam, The Netherlands

Correspondence

Martijn Nagtegaal, Department of Imaging Physics, Delft University of Technology, Lorentzweg 1, 2628 CJ, Delft, The Netherlands.
Email: m.a.nagtegaal@tudelft.nl

Funding information

Medical Delta, Grant/Award Number: Dementia and Stroke 3.0

Purpose: To develop an efficient algorithm for multicomponent MR fingerprinting (MC-MRF) reconstructions directly from highly undersampled data without making prior assumptions about tissue relaxation times and expected number of tissues.

Methods: The proposed method reconstructs MC-MRF maps from highly undersampled data by iteratively applying a joint-sparsity constraint to the estimated tissue components. Intermediate component maps are obtained by a low-rank multicomponent alternating direction method of multipliers (MC-ADMM) including the non-negativity of tissue weights as an extra regularization term. Over iterations, the used dictionary compression is adjusted. The proposed method (k-SPIJN) is compared with a two-step approach in which image reconstruction and multicomponent estimations are performed sequentially and tested in numerical simulations and in vivo by applying different undersampling factors in eight healthy volunteers. In the latter case, fully sampled data serves as the reference.

Results: The proposed method shows improved precision and accuracy in simulations compared with a state-of-art sequential approach. Obtained in vivo magnetization fraction maps for different tissue types show reduced systematic errors and reduced noise-like effects. Root mean square errors in estimated magnetization fraction maps significantly reduce from $13.0\% \pm 5.8\%$ with the conventional, two-step approach to $9.6\% \pm 3.9\%$ and $9.6\% \pm 3.2\%$ with the proposed MC-ADMM and k-SPIJN methods, respectively. Mean standard deviation in homogeneous white matter regions reduced significantly from 8.6% to 2.9% (two step vs. k-SPIJN).

Conclusion: The proposed MC-ADMM and k-SPIJN reconstruction methods estimate MC-MRF maps from highly undersampled data resulting in improved image quality compared with the existing method.

KEYWORDS

MR fingerprinting, MR reconstruction, multicomponent analysis, myelin water imaging, quantitative MRI

Martijn Nagtegaal and Emiel Hartsema contribute equally to this work.

This is an open access article under the terms of the Creative Commons Attribution-NonCommercial-NoDerivs License, which permits use and distribution in any medium, provided the original work is properly cited, the use is non-commercial and no modifications or adaptations are made.

© 2022 The Authors. *Magnetic Resonance in Medicine* published by Wiley Periodicals LLC on behalf of International Society for Magnetic Resonance in Medicine.

1 | INTRODUCTION

MR fingerprinting (MRF)¹ enables the estimation of tissue and system properties by sampling the MR signal in transient states. Conventionally, undersampled images are acquired from which single-component estimates of specific tissue and system parameters are obtained in each voxel, for example, T_1 , T_2 , M_0 , B_1^+ . These parameters are usually estimated by retrieving the best match of a measured time series with a pre-calculated set of reference signals: the so-called dictionary. However, partial volume effects at tissue boundaries and diffuse combinations of tissue structures can lead to mixing of different underlying components. Myelin water imaging (MWI)² is a main research application in which estimating these different tissue components is relevant. MWI is used to detect demyelination caused by multiple sclerosis³ or myelination in the developing human brain.^{4,5} MWI methods such as T_2 -sensitive multi-echo spin echo, GRASE or T_2 -prep,⁶⁻⁸ T_2^* multi-echo gradient echo,⁹ and T_1 , T_2 mcDESPOT¹⁰ result in scan times of more than 10 min when full brain coverage is required.² MWI based on highly undersampled MRF data would make it possible to obtain this clinically relevant information in feasible scan times.

To model such multicomponent effects, the measured MRF signal in a voxel can be represented as a linear combination of the dictionary signals.¹ By definition, however, this multicomponent MRF (MC-MRF) problem is under-determined due to the large number of possible T_1 , T_2 values, even with different forms of voxel-by-voxel regularization,^{11,12} leading to large numbers of components and nonunique solutions. Recently, we proposed a spatial form of regularization to reduce the number of used tissue components. This Sparsity Promoting Iterative Joint NNLS (SPIJN) algorithm was shown to render improved noise resilience in estimated magnetization fraction maps and a small number of identified tissues.¹³

Whereas the conventional single-component dictionary matching is relatively robust to the effects of severe undersampling, MC-MRF generally is not. However, advanced reconstruction schemes can be used to enhance the image quality, exploiting either spatial or temporal similarities of the signals or applying other model-based knowledge. Most of the recently proposed MRF reconstruction methods rely on low-rank properties in the temporal dimension to regularize the inverse problem. For instance, a low-rank space from a central, fully sampled calibration region has been identified.¹⁴ Other methods determined the low-rank singular value decomposition (SVD) space from the simulated signals.¹⁵⁻¹⁹ To further regularize the problem, Zhao et al.²⁰ proposed a maximum likelihood framework to estimate parameter maps of interest during the reconstruction. Likewise, Assländer et al.¹⁸

introduced an alternating direction method of multipliers (ADMM) combining low-rank image reconstruction and dictionary matching, which resulted in improved parameter estimations. However, these methods assumed a single tissue component per voxel, ignoring multicomponent effects.

In this study, we propose a new reconstruction method for obtaining multicomponent parameter estimates directly from MRF k-space data continuing on the previously proposed SPIJN algorithm to obtain SPIJN-MRF estimates from highly undersampled data. The underlying multicomponent inverse problem is solved using a multicomponent alternating direction method of multipliers (MC-ADMM). Since the inverse problem is ill-conditioned, intermediate image reconstruction is performed in a low-rank space. During iterations, the used low-rank compression is updated based on the intermediate results. The proposed method is validated and compared with a more standard approach in simulations and in vivo brain data.

2 | METHODS

2.1 | Reconstruction methods

2.1.1 | Frame-by-frame reconstruction

The MRF image reconstruction problem per time point (excluding regularization or matching) can be mathematically modeled as

$$\hat{x} = \arg \min_{x \in \mathbb{C}^{N_t \times N_n}} \|GF_{N_t}S_{N_t}x - k\|_2^2, \quad (1)$$

where $x \in \mathbb{C}^{N_t \times N_n}$ denotes the MRF (time) series of N_t images consisting of N_n voxels; $k \in \mathbb{C}^{N_t N_k N_s}$ is the acquired k-space data consisting of N_k points per image, and N_s represents the number of (virtual) coils. The linear operators G , F , and S correspond to the non-Cartesian undersampling (interpolation and gridding), Fourier transform, and coil sensitivity encodings, respectively. Essentially, F_{N_t} (F_r) and S_{N_t} (S_r) represent the repetitively applied versions of F and S along the (compressed) time dimension, respectively (see below). However, this problem is highly underdetermined and without further forms of regularization this will result in strong artifacts in the reconstructed images.

2.1.2 | Low-rank inversion (LRI)

The MRF time signal is often modeled based on a low-rank approximation of the MRF-dictionary obtained through a SVD. Let $D \in \mathbb{C}^{N_t \times N_d}$ represent a dictionary consisting of

N_d dictionary atoms, such that the SVD yields $D = U\Sigma V^H$. Here, U and V contain the left and right singular vectors, Σ is a diagonal matrix with singular values, while H denotes Hermitian conjugation.¹⁶ Essentially, $U_r \in \mathbb{C}^{N_r \times r}$, harboring the first r column vectors from U , is applied in MRF as a compression operator, such that $D_r := U_r^H D$ and $x_r := U_r^H x$. As proposed by McGiveny¹⁶ and Assländer et al.¹⁸ (in the Appendix), the compression matrix and Fourier and coil sensitivity operators can be interchanged. After interchanging these operators, the low-rank inversion (LRI) problem can be written as

$$\hat{x}_r = \arg \min_{x_r \in \mathbb{C}^{r \times N_n}} \|GU_r F_r S_r x_r - k\|_2^2, \quad (2)$$

which can be efficiently solved. Optionally, a wavelet regularization term can be included in this step

$$\hat{x}_r = \arg \min_{x_r \in \mathbb{C}^{r \times N_n}} \|GU_r F_r S_r x_r - k\|_2^2 + \sum_{i=1}^r |\tilde{v}_i| \|W(x_{r,i})\|_1, \quad (3)$$

where W is a wavelet operator and \tilde{v}_i the used regularization parameter per time-compressed image $x_{r,i}$. The intensity of these time-compressed images decreases sharply with i and the regularization parameter was adjusted accordingly. As such, the image-wise regularization is based on the intensity over time as $\tilde{v} = \nu \times U_r^H \mathbf{k}_{0,0}$, where $\mathbf{k}_{0,0} \in \mathbb{C}^{N_i}$ are the central positions in k-space of the first virtual coil along time. Effectively, $\nu \in \mathbb{R}_{\geq 0}$ is used as an overall wavelet regularization parameter.

2.1.3 | Multicomponent ADMM reconstruction

We assert that any mixing effects, for example, emanating from partial voluming, can be modeled as a linearly weighted combination of dictionary items. Given certain low-rank images x_r , the weights of the dictionary items can be obtained by solving a non-negative least squares problem:

$$\hat{c} = \arg \min_{c \in \mathbb{R}_{\geq 0}^{N_d \times N_n}} \|P_r(D_r c) - x_r\|_2^2, \quad (4)$$

where $c \in \mathbb{R}_{\geq 0}^{N_d \times N_n}$ are estimated magnetization weights per voxel and dictionary atom, and P_r is applied to represent spatial phase variations. Observe that a single phase is asserted per voxel, independent of the (real-valued) component weights. In our approach, $P \in \mathbb{C}^{N_n}$ was directly calculated based on the LR-solution of (2), using $r = 1$, as

$$P = \frac{x_1}{\text{abs}(x_1)}, \quad (5)$$

(in which the division is done element-wise). Subsequently, P is used to form a linear operator $P_r : \mathbb{R}^{N_r \times N_n} \rightarrow \mathbb{C}^{N_r \times N_n}$. Essentially, P_r sustains a multiplication with P along the temporal dimension.

The full, inverse multicomponent reconstruction problem is defined by combining (2) and (4), leading to:

$$\hat{c} = \arg \min_{c \in \mathbb{R}_{\geq 0}^{N_d \times N_n}} \|GU_r F_r S_r P_r D_r c - k\|_2^2. \quad (6)$$

In order to efficiently solve this non-negative least squares (NNLS) problem, we performed variable splitting similar to Reference 18, in which such splitting was applied for single-component MRF. Accordingly, we rewrote the MC-MRF reconstruction as an augmented Lagrangian minimization problem, in which low-rank images x_r are reconstructed as an intermediate step to split the operators $(GU_r F_r S_r)(P_r D_r)$, and included the wavelet regularization term:

$$\begin{aligned} \hat{x}_r, \hat{c}, \hat{u} = & \arg \min_{x_r, u \in \mathbb{C}^{r \times N_n}, c \in \mathbb{R}_{\geq 0}^{N_d \times N_n}} \left(\frac{1}{2} \|GU_r F_r S_r x_r - k\|_2^2 \right. \\ & + \frac{1}{2} \sum_{i=1}^r |\tilde{v}_i| \|W(x_{r,i})\|_1 \\ & \left. + \frac{\mu}{2} \|P_r D_r c - x_r + u\|_2^2 - \frac{\mu}{2} \|u\|_2^2 \right), \quad (7) \end{aligned}$$

where u is the scaled Lagrange multiplier and μ is the coupling parameter balancing the data and MC-MRF-model consistency.

Subsequently, an alternating directions of multipliers method (ADMM)²¹ was used to solve (7), alternating between:

$$\begin{aligned} \hat{x}_r = \arg \min_{x_r \in \mathbb{C}^{r \times N_n}} & \frac{1}{2} \|GU_r F_r S_r x_r - k\|_2^2 \\ & + \frac{\mu}{2} \|P_r D_r \hat{c} - \hat{x}_r + \hat{u}\|_2^2 + \sum_{i=1}^r |\tilde{v}_i| \|W(x_{r,i})\|_1, \quad (8a) \end{aligned}$$

$$\hat{c} = \arg \min_{c \in \mathbb{R}_{\geq 0}^{N_d \times N_n}} \frac{\mu}{2} \|D_r c - P_r^H (\hat{x}_r + \hat{u})\|_2^2, \quad (8b)$$

$$\hat{u} = u + \hat{x}_r - P_r D_r \hat{c}, \quad (8c)$$

until convergence was reached. Specifically, we solved Equation (8a) using a preconditioned primal-dual hybrid gradient solver^{22,23} with a relative convergence tolerance of 0.5%. Equation (8b) was solved using the NNLS algorithm.²⁴ Essentially, the proposed low-rank multicomponent ADMM (MC-ADMM) estimates the MRF image sequence as a non-negative linear combination of dictionary atoms and corresponding weights (magnetization maps). The steps followed in the algorithm are depicted in Figure 1, top.

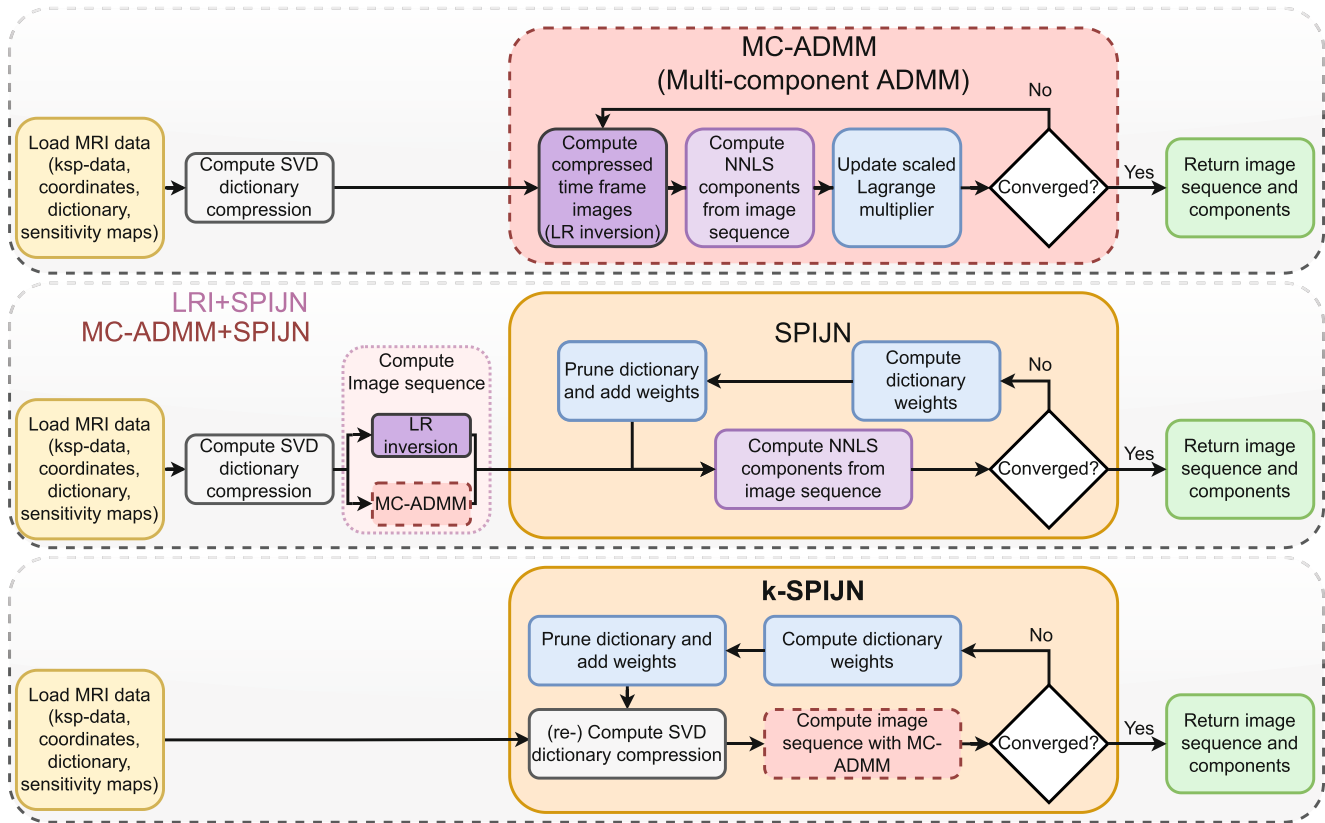


FIGURE 1 Schematic description of the proposed reconstruction schemes. The upper row visualizes the proposed multicomponent ADMM, including the non-negativity constraint on the component weights, which is integrated into the performed MRF reconstruction. MC-ADMM reconstruction (red box) is used as part of the second and third reconstruction schemes. The center row shows the combination of the previously proposed SPIJN¹³ method applied to LR inversion images (LRI+SPIJN) and MC-ADMM reconstructed images (MC-ADMM+SPIJN). The last flowchart (k-SPIJN) combines the joint-sparsity constraint from SPIJN with the MC-ADMM solver to obtain multicomponent magnetization maps.

2.1.4 | Joint-sparsity constraint implementation (SPIJN)

To further restrict the solution space, we introduce the joint-sparsity constraint that was already implemented in the SPIJN algorithm.¹³ The SPIJN algorithm was originally developed for multicomponent estimation taking *reconstructed*, presumed artifact-free MRF images as its input.

The joint (component) sparsity constraint limits the number of tissue components, that is, in a voxel and spatially, resulting in a small number of non-zero magnetization fraction maps. The sparsity term was implemented by combining dictionary reweighting²⁵ and ℓ_1^2 -regularization²⁶ in an iterative process to reduce the number of used dictionary atoms. SPIJN repeatedly solves a modified version of Equation (4):

$$\hat{c} = \arg \min_{c \in \mathbb{R}_{\geq 0}^{N_c \times N_n}} \|\tilde{D}_r c - P_r^H \tilde{x}_r\|_2^2, \quad (9)$$

during which $N_c = \sum_{i=1}^N \|c_i\|_0$ reduces over iterations while the variables \tilde{D}_r and \tilde{x}_r are updated according to

$$w_i = \|\mathbf{c}^i\|_2 + \epsilon, \quad \forall i \in \{1, \dots, N_c\}, \quad (10a)$$

$$W = \text{diag}(\mathbf{w}^{1/2}), \quad (10b)$$

$$\tilde{D}_r = \begin{bmatrix} D_r W \\ \lambda \mathbf{1}^T \end{bmatrix}, \quad (10c)$$

$$\tilde{x}_r = \begin{bmatrix} P_r^H(x_r) \\ \mathbf{0}^T \end{bmatrix}, \quad (10d)$$

where λ and $\epsilon = 10^{-4}$ are the SPIJN and reweighting regularization parameters respectively. Note that in Equations (10c), (10d), the tilde symbol is used to indicate intermediate representations of concerned variables, which are updated during iterations. While doing so, the

ℓ_1^2 regularization is imposed by adding a row of λ 's to the reweighted dictionary $D_r W$ and zeros to $P_r^H(x_r)$. Not used dictionary atoms will be assigned a zero weight. However, computationally it is more efficient to remove these atoms from the dictionary and further calculations, a processing step we refer to as pruning.

We applied this algorithm to image series reconstructed by LRI and the MC-ADMM, referred to as LRI+SPIJN and MC-ADMM+SPIJN reconstructions, which is graphically depicted in Figure 1, center flowchart. In our previous work, we performed the multicomponent estimation only after image reconstruction of fully sampled data or undersampled data from longer acquisitions, involving markedly longer scan times.

2.1.5 | Simultaneous image reconstruction and joint-sparsity multicomponent parameter estimation

Isolating the dictionary reweighting and pruning steps facilitates to integrate them in a new iterative algorithm in which image reconstruction and joint-sparsity multicomponent parameter estimation directly use the k-space data as input. Specifically, the restricted dictionary D_S was used to update the SVD-compression matrix U_r for improved compression efficiency of the remaining dictionary signals. Effectively we are solving the following minimization problem:

$$\hat{c}, \hat{U}_r = \arg \min_{c \in \mathbb{R}_{\geq 0}^{N_d \times N_r}, U_r \in \mathbb{C}^{N_r \times r}} \|GU_r F_r S_r P_r D_r c - k\|_2^2 + \sum_{i=1}^N \|c_i\|_0, \quad (11)$$

As such, the MC-ADMM was employed to obtain multicomponent estimates in an inner loop, while dictionary reweighting and compression were performed in the outer loop of our algorithm. This novel approach will be referred to as k-SPIJN and is summarized in Figure 1, bottom flowchart. A step-by-step description of the proposed reconstruction method can be found in the Supporting Information, Algorithm 1.

2.2 | Experimental setup

All the methods were programmed in Python using the main parts of the SigPy library.²⁷ Computations were performed on an Intel E5-2683 CPU based on a single core implementation and using NVIDIA GTX 1080 Ti GPU.

All experiments were performed with a gradient spoiled SSFP MRF acquisition²⁸ using a flip angle train of length 400 (see Supporting Information Figure S1)²⁹ with

fixed TR=15 ms. Dictionary signals were simulated with extended phase graphs³⁰ using a T_1 ranging from 100 ms to 5 s and T_2 from 10 ms to 3 s, applying a logarithmic stepsize of 5%.

Data were normalized with respect to the ℓ_2 -norm of the k-space data. All experiments were performed with an initial rank of $r = 10$. Visible effects of wavelet regularization were kept to a minimum while reducing noise-like artifacts using an experimentally determined value of $\nu = 5 \times 10^{-6}$.

2.2.1 | Numerical experiments

Numerical experiments were performed with the Brain-Web phantom as ground truth³¹ making use of the provided partial volume segmentations of white matter (WM), gray matter (GM), and CSF. Time frame images were computed after which simulated coil sensitivity maps were applied and noise was added $\left(\text{SNR} = \frac{\text{image mean}}{\text{standard deviation}} = 70\right)$. Subsequently, k-space data were generated by performing a Fourier transform, which was then undersampled with a constant density spiral at an undersampling factor of 1/32.

Experiments were performed with different ADMM-coupling parameter values μ , while the root mean square error (RMSE) in estimated mean T_1 , T_2 , and M_0 (as defined below) and signal residual were evaluated during iterations.

2.2.2 | In vivo experiments

After obtaining informed consent and with approval of the local Ethics board, eight volunteers were scanned on a 3.0 T Philips Ingenia (Philips, Best, The Netherlands) scanner with a 32-channel head coil, SVD-compressed to five virtual coils³² after ESPIRiT coil estimation.³³ A constant density spiral sampling pattern, FOV of 240 mm \times 240 mm, in plane resolution of 1 mm \times 1 mm and 5 mm slice thickness were used. A single brain slice was imaged. Data were acquired using spiral sampling of 1/32 of the fully sampled k-space per spiral arm, having a readout duration of 6.5 ms; incremental rotations of 360°/32 were applied with each flip angle. Furthermore, acquisitions were performed with 1, 5, and 32 flip angle train repetitions, resulting in acquisition times of 6 s, 42 s, and 4:48 min. Undersampled data were reconstructed with LRI+SPIJN, MC-ADMM+SPIJN, and k-SPIJN with SPIJN-regularization $\lambda = 0.05$. Additionally, fully sampled time frame images were reconstructed with a SENSE reconstruction³⁴ and a SPIJN segmentation was obtained serving as a reference. For all estimations, tissue types

were identified based on the following relaxation times: myelin water (MW): $T_1 < 800$ ms, $T_2 < 40$ ms; white matter (WM): 800 ms $< T_1 < 1200$ ms, 40 ms $< T_2 < 100$ ms; gray matter (GM): 1200 ms $< T_1 < 1700$ ms, 45 ms $< T_2 < 100$ ms; and CSF: $T_1 > 1750$ ms. When multiple components were estimated for one tissue type, magnetization fractions were summed and a weighted average of relaxation times was computed.

To assess structural differences, fully sampled (partial volume) segmentations (A) and segmentations from undersampled data (B) were compared using the Fuzzy Tanimoto coefficient:³⁵

$$TC_F = \frac{\sum_{i=1}^{N_v} \text{MIN}(A_i, B_i)}{\sum_{i=1}^{N_v} \text{MAX}(A_i, B_i)}, \quad (12)$$

where N_v is the number of non-zero voxels. Additionally, the RMSE measure was calculated:

$$RMSE = \sqrt{\frac{\sum_{i=1}^{N_v} (A_i - B_i)^2}{N_v}}, \quad (13)$$

across the brain per tissue type. To quantify the image quality of segmentations, the standard deviation (SD) in a homogeneous frontal white matter region (size 10×20 voxels) was also calculated for MW, GM, and WM. A Wilcoxon signed rank test was performed to statistically assess the differences between error measures, while a p -value < 0.05 was considered significant.

3 | RESULTS

3.1 | Numerical experiments

Results of numerical simulations showing the effect of the ADMM-coupling parameter μ are depicted in Supporting Information Figure S2. A high μ reduces the convergence speed. Simultaneously, the individual RMSE in mean T_1 and T_2 increases for too small or large coupling parameters and do not exhibit a monotonic relation. Based on these findings, we chose to use $\mu = 2 \cdot 10^{-3}$ in further experiments.

In Figure 2 relative error maps are shown comparing the segmentations obtained from LRI+SPIJN, MC-ADMM+SPIJN, and k-SPIJN reconstructions. Only small effects are observable in CSF segmentations (RMSE ranging from 1.7% to 2.7%), but larger differences are noticeable for WM and GM (RMSE up to 29.9%). Additionally, LRI+SPIJN yields highly deviating relaxation times, while the proposed methods result in smaller errors of the relaxation times.

3.2 | In vivo experiments

The computation time for the LRI+SPIJN was 4:34 min (maximum memory usage: 5 GB), for MC-ADMM+SPIJN 45:49 min (11 GB), and for k-SPIJN 1:42:51 h (16 GB).

Figure 3 shows estimated multicomponent estimations for one subject. Figure 4 shows similar difference maps for a second subject. From these maps, it can be observed that differences between fully sampled and undersampled scans are reduced with k-SPIJN and MC-ADMM+SPIJN. However, small structural biases can still be observed.

A further quantitative comparison between reconstruction methods is collated in Figure 5, showing the TC_F and RMSE across the component images, the SD in a homogeneous, frontal WM region with different undersampling factors, and estimated T_1 and T_2 relaxation times for the different methods and undersampling factors.

The proposed MC-ADMM+SPIJN and k-SPIJN method accurately estimated fraction maps from 1/32 undersampled data: mean RMSE of $9.6\% \pm 3.9\%$ and $9.6\% \pm 3.2\%$. This is a significant improvement compared with the conventional LRI+SPIJN approach: mean RMSE $13.0\% \pm 5.8\%$. For an undersampling of 5/32, the respective mean RMSEs were $9.9\% \pm 5.4\%$, $7.3\% \pm 2.5\%$, and $7.8\% \pm 2.4\%$ for LRI+SPIJN, MC-ADMM+SPIJN, and k-SPIJN, again showing a significant difference between LRI+SPIJN and the two proposed methods. An overview of performed tests and results is given in Table S2 in the Supporting Information.

Differences between k-SPIJN and MC-ADMM were mostly not significant with respect to the FT_C and RMSE, but significant differences were observed with respect to the SD in WM regions, both for 1/32 and 5/32 undersampling.

Estimated relaxation times for MC-ADMM+SPIJN and k-SPIJN were highly similar irrespective of the used undersampling factor and in line with reference values.³⁶ For LRI+SPIJN, extra components between WM-GM and GM-CSF relaxation times were identified, resulting in 12 components on average, in which cases MC-ADMM and k-SPIJN estimated nine and eight components on average. The largest spread in estimated relaxation times was observed for CSF, which did not seem to effect the estimated magnetization fraction maps.

4 | DISCUSSION

We proposed two new reconstruction methods for MRF data, tailored to the estimation of multicomponent

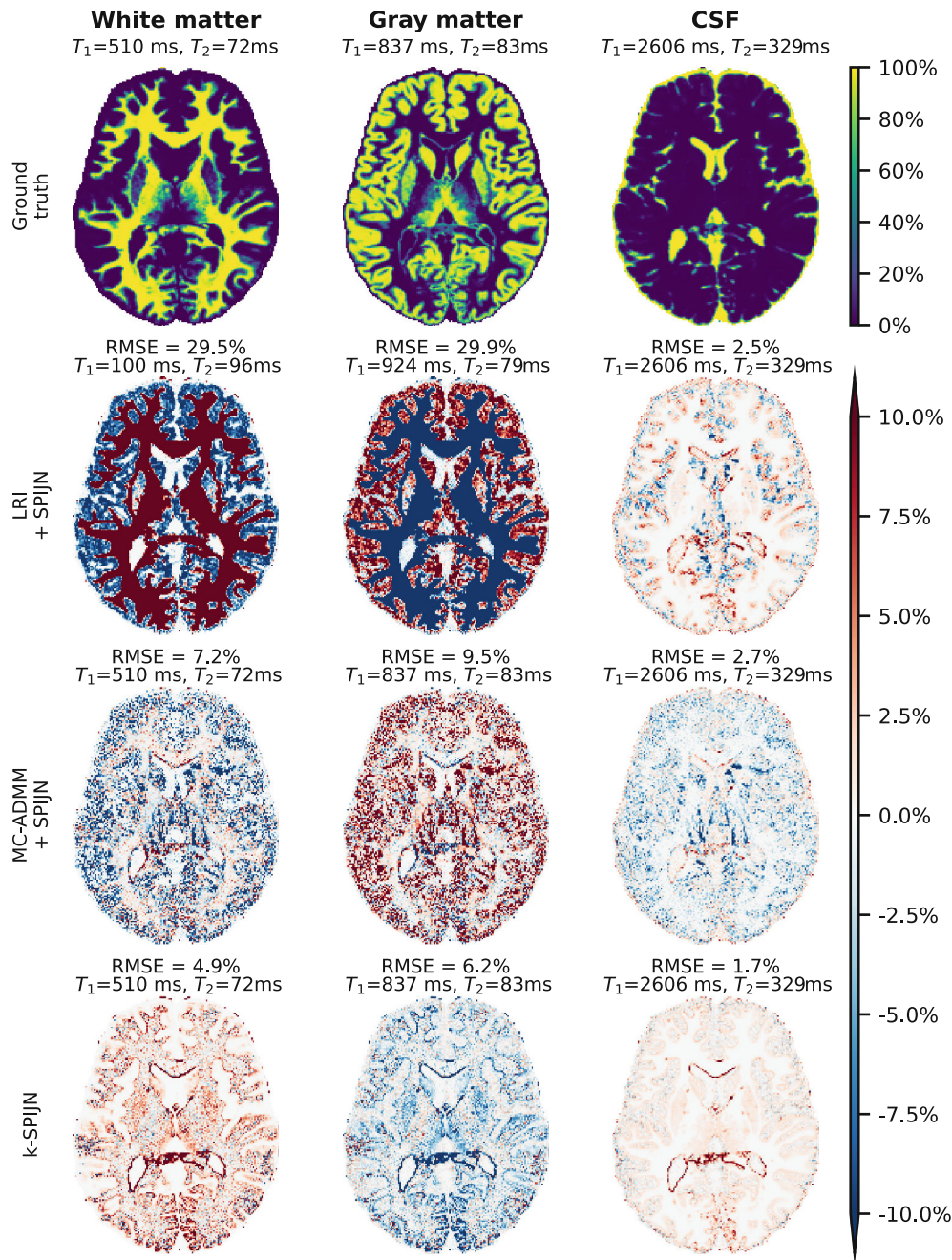


FIGURE 2 Error maps for obtained multicomponent tissue segmentations using different reconstruction methods (bottom three rows). A numerical BrainWeb phantom was used as ground truth (upper row) for which an MRF sequence of length 200 was generated. RMSE is reported over the whole brain. Ground truth (top row) and estimated relaxation times are reported above each map.

magnetization maps. The proposed MC-ADMM and k-SPIJN methods were assessed in simulations and in vivo data. As reference we used numerical ground truth data in the simulations and conventional multicomponent estimations after traditional image reconstruction with the fully sampled in vivo data.

We found in the numerical simulations that the MC-ADMM-SPIJN and k-SPIJN facilitated accurate magnetization fraction estimation for a short (200 readouts) MRF sequence, while the state-of-art LRI+SPIJN yielded markedly poorer outcomes (see Figure 2). In in vivo experiments, this shorter sequence of length 200 was not used (sequence length 400 was used), as the improved

image quality in all reconstruction was preferred over the reduced scan time.

The proposed methods yielded MW, WM, GM, and CSF maps from in vivo data for single spiral readouts (1/32) that closely resembled the reference. The LRI+SPIJN method showed larger deviations in this respect. Furthermore, we observed that the main improvement from MC-ADMM+SPIJN to k-SPIJN is a reduction in noise-like patterns (see Figures 3 and 5; std. estimates). This came at the cost of increased computation times for both the MC-ADMM+SPIJN and k-SPIJN methods compared with the LRI+SPIJN reconstruction. These increased computation times are mainly caused by the

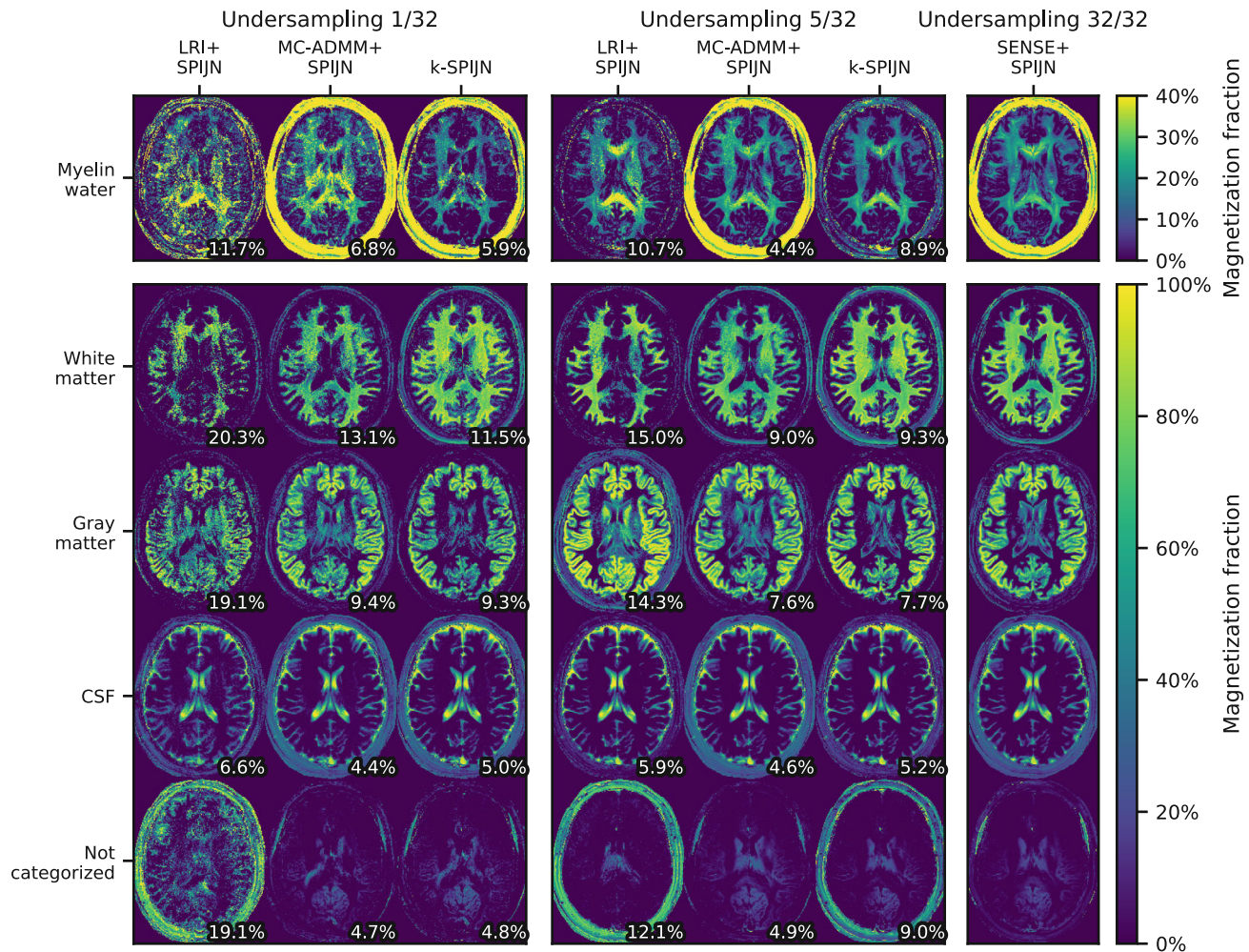


FIGURE 3 Estimated magnetization fraction maps from single slice data of one volunteer acquired with different undersampling factors applying different reconstruction methods. Estimated SPIJN-MRF maps with undersampling factors 1/32 and 5/32 are shown for the LRI+SPIJN, the proposed MC-ADMM+SPIJN and k-SPIJN reconstructions. Fully sampled MRF data with SENSE reconstruction and SPIJN-MRF estimation shown on the right serve as a reference. On the lower right side of each image, the RMSE compared with the fully sampled data is given.

many NNLS optimizations that are performed. Notably, these optimizations were not performed in parallel in the current implementation. Obviously, doing so could drastically reduce the calculation times.^{37,38}

The main novelty in the MC-ADMM reconstruction essentially lies in imposing a voxel-wise temporal constraint, while reconstructing LR-images from the k-space data in an iterative process. This constrains the reconstructed LR-images to a non-negative combination of dictionary atoms, which is more restrictive than standard LR-reconstruction,^{19,39} in which only the dimension of the solution space is reduced. At the same time, such a constraint still allows for multicomponent estimations, with or without a joint-sparsity constraint,^{11,12,40} which is not possible with methods that benefit from a dictionary matching based constraint,^{18,20,41,42} assuming a single tissue per voxel.

By regularizing the total number of T_1 , T_2 -components used, the proposed k-SPIJN reconstruction adds a spatial constraint leading to a further improvement in image quality.

A wavelet regularization term with a relatively small regularization value was used in all the reconstructions to suppress small spiral artifacts in the low-rank images. The low-rank image reconstruction (Equation 3) can be easily expanded to 3D-acquisitions or to include other regularization terms^{19,43} and spiral blurring correction methods.⁴⁴⁻⁴⁶

Some limitations of the performed work can be identified. A limitation of the SPIJN and k-SPIJN algorithms is that potentially important components could be discarded in early iterations. This risk is limited by not rejecting too many components and only refute those that have very small weight. Incidentally, we have not observed in any

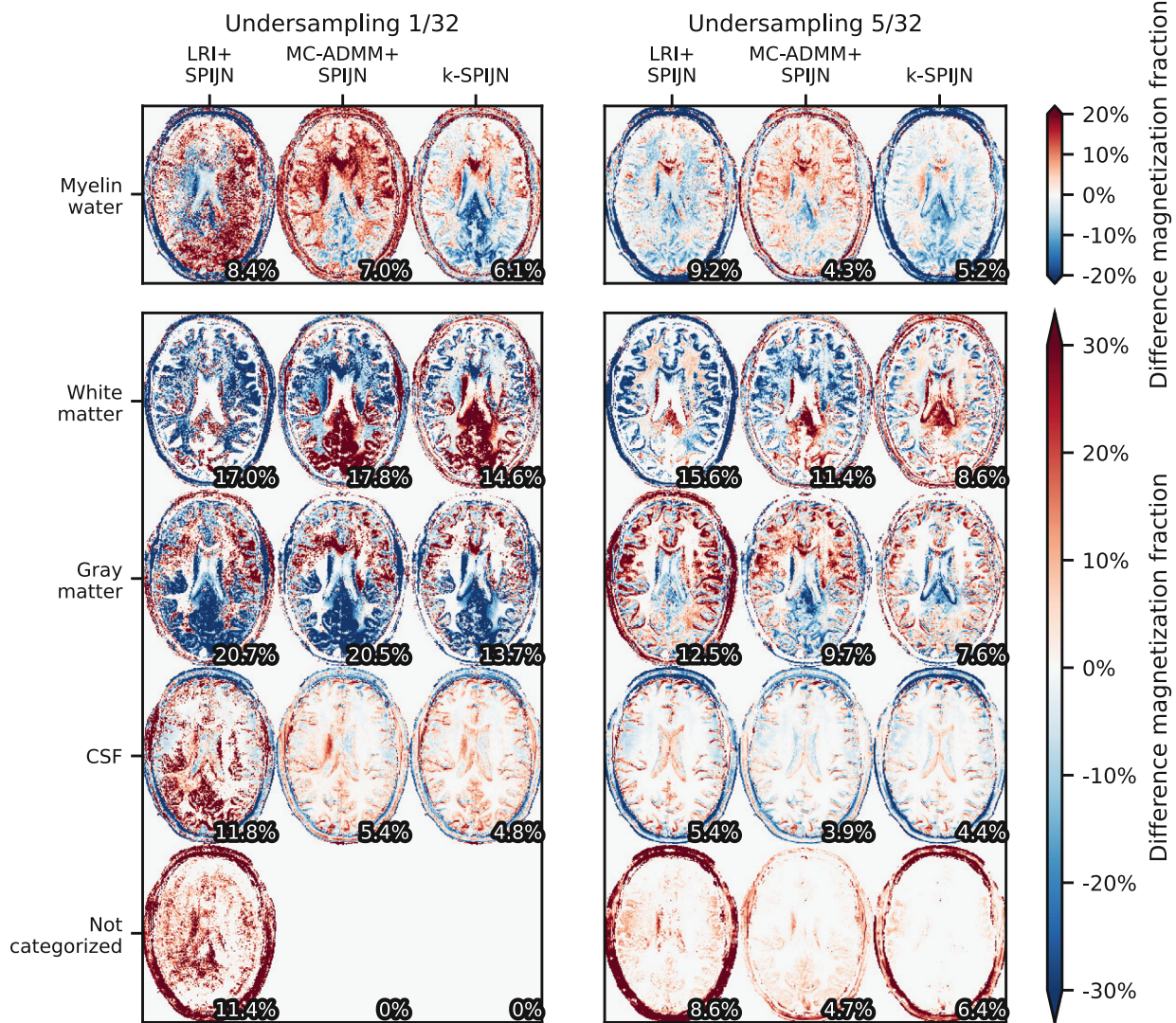


FIGURE 4 Differences in estimated magnetization fraction maps from single slice data of a second volunteer acquired with different undersampling factors applying different reconstruction methods. Difference maps for estimated SPIJN-MRF maps with undersampling factors 1/32 and 5/32 are shown for the LRI+SPIJN, the proposed MC-ADMM+SPIJN, and k-SPIJN reconstructions. On the lower right of each image, the RMSE compared with the fully sampled data is indicated.

of our experiments that key components (e.g., reflecting WM/GM or myelin water) were discarded at an early stage.

In the performed experiments, no corrections for B_1^+ inhomogeneities were included because B_1^+ was rather homogeneous. However, in the multicomponent estimation, a (separately acquired) B_1^+ -map could be included to fixate B_1^+ per voxel. Modeling B_1^+ in the dictionary may require applying a higher rank in the compression.

Although relaxation times and visual appearance of identified myelin water like components are in agreement with the literature,² comprehensive validation with conventional MWI methods is a subject of further study and is required to study potential biases, caused by, for

example, the proposed algorithm, magnetization transfer effects or MRF sequence choice. Observe that such a study is increasingly feasible due to the achieved reduction in scan time and reconstruction quality. Further research should therefore also look into the sensitivity of different flip angle patterns to multicomponent effects and how this can improve MWI, for example, by using multiple inversion pulses⁴⁷ or model-based sequence optimization.^{48,49}

5 | CONCLUSION

New MC-ADMM+SPIJN and k-SPIJN algorithms facilitate accurate estimation of magnetization fraction maps

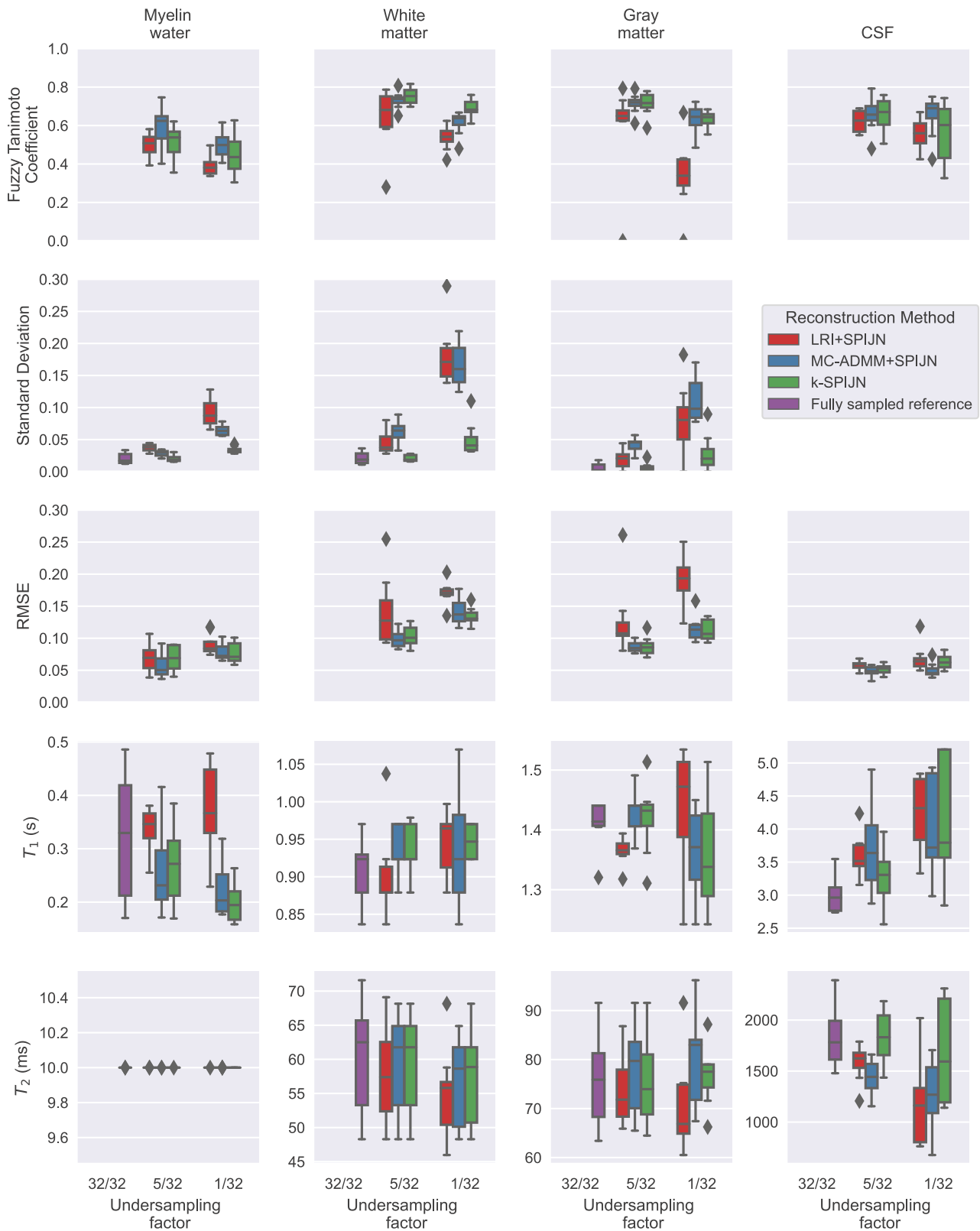


FIGURE 5 Comparison of different reconstructions based on undersampled data of eight in vivo scans. The Fuzzy Tanimoto coefficient and RMSE were calculated over the complete components with respect to the fully sampled (32/32) SENSE+SPIJN reconstruction. The SD of the magnetization fraction was calculated in a frontal white matter region for all acquisitions, including the fully sampled data. As no CSF was identified in the frontal WM region, the graph showing the SD of this component is left out. The distribution of estimated T_1 and T_2 relaxation times per tissue is shown in the lower two rows. Mean values and SDs can be found in Table S1 of the Supporting Information.

from highly undersampled MRF k-space data. The generated in vivo maps show close resemblance to fully sampled reference data, while scan times of less than 10 s per slice can be achieved.⁵⁰

ACKNOWLEDGMENT

The authors want to thank Peter Börnert, Peter Koken, and Mariya Doneva for help with acquisitions and fruitful discussions.

FUNDING INFORMATION

This research was funded by the Medical Delta consortium, a collaboration between TU Delft, Erasmus MC, and Leiden University Medical Center.


CONFLICT OF INTEREST

The author declares that there is no conflict of interest that could be perceived as prejudicing the impartiality of the research reported.

DATA AVAILABILITY STATEMENT

The full implementation of the proposed MC-ADMM and k-SPIJN methods can be found at <https://github.com/imphys/MC-MRF>

ORCID

Martijn Nagtegaal  <https://orcid.org/0000-0002-6563-865X>

Kirsten Koolstra  <https://orcid.org/0000-0002-7873-1511>

REFERENCES

- Ma D, Gulani V, Seiberlich N, et al. Magnetic resonance fingerprinting. *Nature*. 2013;495:187-192. <http://www.nature.com/articles/nature11971>
- Piredda GF, Hilbert T, Thiran JP, Kober T. Probing myelin content of the human brain with MRI: a review. *Magn Reson Med*. 2021;85:627-652.
- Laule C, Vavasour IM, Moore GRW, et al. Water content and myelin water fraction in multiple sclerosis. *J Neurol*. 2004;251:284-293.
- Chen Y, Chen MH, Baluyot KR, Potts TM, Jimenez J, Lin W. MR fingerprinting enables quantitative measures of brain tissue relaxation times and myelin water fraction in the first five years of life. *NeuroImage*. 2019;186:782-793. <http://www.sciencedirect.com/science/article/pii/S1053811918321190>
- Cencini M, Lancione M, Biagi L, et al. Myelin water fraction mapping in developing children using magnetic resonance fingerprinting. *Proc Intl Soc Mag Reson Med*. 2021;29:0165. <https://cds.ismrm.org/protected/21MPresentations/abstracts/0165.html>
- Whittall KP, Mackay AL, Graeb DA, Nugent RA, Li DKB, Paty DW. In vivo measurement of T2 distributions and water contents in normal human brain. *Magn Reson Med*. 2000;37:34-43.
- Prasloski T, Rauscher A, MacKay AL, et al. Rapid whole cerebrum myelin water imaging using a 3D GRASE sequence. *NeuroImage*. 2012;63:533-539. <http://www.sciencedirect.com/science/article/pii/S1053811912006805>
- Oh J, Han ET, Pelletier D, Nelson SJ. Measurement of in vivo multi-component T2 relaxation times for brain tissue using multi-slice T2 prep at 1.5 and 3 T. *Magnet Reson Imaging*. 2012;24:33-43. <http://linkinghub.elsevier.com/retrieve/pii/S0730725X05003097>
- Du YP, Chu R, Hwang D, et al. Fast multislice mapping of the myelin water fraction using multicompartment analysis of T decay at 3T: a preliminary postmortem study. *Magn Reson Med*. 2007;58:865-870.
- Deoni SCL, Rutt BK, Arun T, Pierpaoli C, Jones DK. Gleaning multicomponent T1 and T2 information from steady-state imaging data. *Magn Reson Med*. 2008;60:1372-1387.
- McGivney D, Deshmane A, Jiang Y, et al. Bayesian estimation of multicomponent relaxation parameters in magnetic resonance fingerprinting: Bayesian MRF. *Magn Reson Med*. 2018;80:159-170.
- Tang S, Fernandez-Granda C, Lannuzel S, et al. Multicomponent magnetic resonance fingerprinting. *Inverse Probl*. 2018;34:094005. <http://stacks.iop.org/0266-5611/34/i=9/a=094005?key=crossref.7b2cd4f80e39f5c6959df77cbca603ca>
- Nagtegaal MA, Koken P, Amthor T, Doneva M. Fast multi-component analysis using a joint sparsity constraint for MR fingerprinting. *Magn Reson Med*. 2020;83:521-534.
- Doneva M, Amthor T, Koken P, Sommer K, Börnert P. Matrix completion-based reconstruction for undersampled magnetic resonance fingerprinting data. *Magn Reson Imaging*. 2017;41:41-52. <https://linkinghub.elsevier.com/retrieve/pii/S0730725X17300383>
- Doneva M, Börnert P, Eggers H, Stehning C, SÉNÉGAS J, Mertins A. Compressed sensing reconstruction for magnetic resonance parameter mapping. *Magn Reson Med*. 2010;64:1114-1120.
- McGivney DF, Pierre E, Ma D, et al. SVD compression for magnetic resonance fingerprinting in the time domain. *IEEE Trans Med Imaging*. 2014;33(12):2311-2322.
- Tamir JI, Uecker M, Chen W, et al. T2 shuffling: sharp, multi-contrast, volumetric fast spin-echo imaging. *Magn Reson Med*. 2017;77:180-195.
- Assländer J, Cloos MA, Knoll F, Sodickson DK, Hennig J, Lantani R. Low rank alternating direction method of multipliers reconstruction for MR fingerprinting: low rank ADMM reconstruction. *Magn Reson Med*. 2018;79:83-96.
- Lima da Cruz G, Bustin A, Jaubert O, Schneider T, Botnar RM, Prieto C. Sparsity and locally low rank regularization for MR fingerprinting. *Magn Reson Med*. 2019;81:3530-3543.
- Zhao B, Setsompop K, Ye H, Cauley SF, Wald LL. Maximum likelihood reconstruction for magnetic resonance fingerprinting. *IEEE Trans Med Imaging*. 2016;35:1812-1823. <https://ieeexplore.ieee.org/document/7412760>
- Boyd S, Parikh N, Chu E, Peleato B, Eckstein J. Distributed optimization and statistical learning via the alternating direction method of multipliers. *Found Trends Mach Learn*. 2010;3:1-122.
- Chambolle A, Pock T. A first-order primal-dual algorithm for convex problems with applications to imaging. *J Math Imaging Vis*. 2011;40:120-145.

23. Ong F, Uecker M, Lustig M. Accelerating non-Cartesian MRI reconstruction convergence using k-space preconditioning. *IEEE Trans Med Imaging*. 2020;39:1646-1654.
24. Lawson CL, Hanson RJ. Solving least squares problems; 1974.
25. Tropp JA, Gilbert AC, Strauss MJ. Algorithms for simultaneous sparse approximation. Part I: Greedy pursuit. *Signal Process*. 2006;86:572-588. <http://linkinghub.elsevier.com/retrieve/pii/S0165168405002227>
26. Foucart S, Koslicki D. Sparse recovery by means of nonnegative least squares. *IEEE Signal Process Lett*. 2014;21:498-502. <http://ieeexplore.ieee.org/document/6750023/>
27. Ong F, Lustig M. SigPy: a python package for high performance iterative reconstruction. Proceedings of the International Society of Magnetic Resonance in Medicine; 2019:4819; Montréal, QC.
28. Jiang Y, Ma D, Seiberlich N, Gulani V, Griswold MA. MR fingerprinting using fast imaging with steady state precession (FISP) with spiral readout. *Magn Reson Med*. 2015;74:1621-1631.
29. Sommer K, Amthor T, Koken P, Meineke J, Doneva M. Determination of the optimum pattern length of MRF sequences. *Proc Intl Soc Mag Reson Med*. 2017;25:1491. <https://cds.ismrm.org/protected/17MPresentations/abstracts/1491.html>
30. Hennig J. Multiecho imaging sequences with low refocusing flip angles. *J Magn Reson*. 1988;78:397-407. <http://linkinghub.elsevier.com/retrieve/pii/002223648890128X>
31. Collins DL, Zijdenbos AP, Kollokian V, et al. Design and construction of a realistic digital brain phantom. *IEEE Trans Med Imaging*. 1998;17:463-468.
32. Buehrer M, Pruessmann KP, Boesiger P, Kozerke S. Array compression for MRI with large coil arrays. *Magn Reson Med*. 2007;57:1131-1139.
33. Uecker M, Lai P, Murphy MJ, et al. ESPIRiT—an eigenvalue approach to autocalibrating parallel MRI: Where SENSE meets GRAPPA. *Magn Reson Med*. 2014;71:990-1001. <http://onlinelibrary.wiley.com/doi/abs/10.1002/mrm.24751>
34. Pruessmann KP, Weiger M, Scheidegger MB, Boesiger P. SENSE: Sensitivity encoding for fast MRI. *Magn Reson Med*. 1999;42:952-962.
35. Crum WR, Camara O, Hill DLG. Generalized overlap measures for evaluation and validation in medical image analysis. *IEEE Trans Med Imaging*. 2006;25:1451-1461.
36. Bojorquez JZ, Bricq S, Acquitier C, Brunotte F, Walker PM, Lalande A. What are normal relaxation times of tissues at 3T? *Magn Reson Imaging*. 2017;35:69-80. <http://linkinghub.elsevier.com/retrieve/pii/S0730725X16301266>
37. Benthem MHV, Keenan MR. Fast algorithm for the solution of large-scale non-negativity-constrained least squares problems. *J Chemom*. 2004;18(10):441-450. <https://onlinelibrary.wiley.com/doi/abs/10.1002/cem.889>.
38. Luo Y, Duraiswami R. Efficient parallel nonnegative least squares on multicore architectures. *SIAM J Sci Comput*. 2011;33:2848-2863.
39. Zhao B, Setsompop K, Adalsteinsson E, et al. Improved magnetic resonance fingerprinting reconstruction with low-rank and subspace modeling. *Magn Reson Med*. 2018;79:933-942.
40. Nagtegaal MA, Hermann I, Weingärtner SD, de Bresser J, Vos FM. Detection of small cerebral lesions using multi-component MR Fingerprinting with local joint sparsity. *Proc Intl Soc Mag Reson Med*. 2020;28:1828.
41. Pierre EY, Ma D, Chen Y, Badve C, Griswold MA. Multi-scale reconstruction for MR fingerprinting. *Magn Reson Med*. 2016;75:2481-2492.
42. Cline CC, Chen X, Mailhe B, et al. AIR-MRF: accelerated iterative reconstruction for magnetic resonance fingerprinting. *Magn Reson Imaging*. 2017;41:29-40. <http://www.sciencedirect.com/science/article/pii/S0730725X1730125X>
43. Bustin A, GLd C, Jaubert O, Lopez K, Botnar RM, Prieto C. High-dimensionality undersampled patch-based reconstruction (HD-PROST) for accelerated multi-contrast MRI. *Magn Reson Med*. 2019;81:3705-3719.
44. Börnert P, Schomberg H, Aldefeld B, Groen J. Improvements in spiral MR imaging. *MAGMA*. 1999;9:29-41.
45. Coronado R, Cruz G, Castillo-Passi C, et al. A spatial off-resonance correction in spirals for magnetic resonance fingerprinting. *IEEE Trans Med Imaging*. 2021;40:3832-3842.
46. Koolstra K, Webb AG, Veeger TTJ, Kan HE, Koken P, Börnert P. Water-Fat separation in spiral magnetic resonance fingerprinting for high temporal resolution tissue relaxation time quantification in muscle. *Magn Reson Med*. 2020;84:646-662.
47. Cui D, Hui ES, Cao P. A multi-inversion-recovery magnetic resonance fingerprinting for multi-compartment water mapping. *Magn Reson Imaging*. 2021;81:82-87. <https://www.sciencedirect.com/science/article/pii/S0730725X2100093X>
48. Heesterbeek DGJ, Vos F, van Gijzen M, Nagtegaal MA. Sequence optimisation for multi-component analysis in magnetic resonance fingerprinting. *Proc Intl Soc Mag Reson Med*. 2021;29:1561. <https://index.miramsmart.com/ISMRM2021/PDFfiles/1561.html>
49. Zhao B, Haldar JP, Liao C, et al. Optimal experiment design for magnetic resonance fingerprinting: Cramér-Rao bound meets spin dynamics. *IEEE Trans Med Imaging*. 2018;38:844-861. <https://ieeexplore.ieee.org/document/8481484>
50. Nagtegaal M, Hartsema E, Multi-component MRF reconstruction; 2022.

SUPPORTING INFORMATION

Additional supporting information may be found in the online version of the article at the publisher's website.

Data S1: Supporting information

Algorithm 1: The proposed MC-MRF reconstruction algorithm k-SPIJN with joint-sparsity and low-rank constraints.

Table S1: Descriptive statistics from the box plots as shown in Figure 5.

Table S2: Results as obtained from Wilcoxon signed rank tests to compare the different methods for different undersampling factors and error measures. Gray rows show significant results.

Figure S1: The used flip angle pattern²⁹ of length 400. For the simulations a shorter version of length 200 (dashed line) was used.

Figure S2: RMSE in T_1 , T_2 , M_0 and the residual of the fit as a function of iteration number for different values of the ADMM coupling parameter μ . The numerical

BrainWeb phantom was used as ground truth. Errors were evaluated over the complete image. Geometric mean T_1 and T_2 were derived from the obtained component maps. $\|GF_{N_i} S_{N_i} x - k\|_2$ denotes the difference between reconstructed image series and k-space signal.

How to cite this article: Nagtegaal M, Hartsema E, Koolstra K, Vos F. Multicomponent MR fingerprinting reconstruction using joint-sparsity and low-rank constraints. *Magn Reson Med.* 2023;89:286-298. doi: 10.1002/mrm.29442